# Huntingtin aggregates and mitochondrial pathology in skeletal muscle but not heart of late-stage, R6/2 mice

Kerstin Kojer[1], Tanja Hering[1], Chantal Bazenet[2], Andreas Weiss[2], Frank Herrmann[2], Jan-Willem Taanman[3], and Michael Orth[1]

[1]Dept of Neurology, Ulm University, Ulm, Germany; [2]Evotec AG, Hamburg, Germany; [3]Dept of Clinical and Movement Neurosciences, Queen Square Institute of Neurology, UCL, London, United Kingdom

**Contact for correspondence**

Michael Orth, M.D., Ph.D.

Department of Neurology, Ulm University Hospital

Oberer Eselsberg 45/1

89081 Ulm, Germany

e-mail: michael.orth@uni-ulm.de

Tel: +49-731 50063095; Fax: +49-731 50063082

***Abstract***

BACKGROUND: Cell or tissue specific background may influence the consequences of expressing the Huntington's disease (HD) mutation. Aggregate formation is known to occur in skeletal muscle, but not heart of the R6/2 fragment HD model.

OBJECTIVE: We asked whether aggregate formation and the expression and subcellular localization of huntingtin species was associated with mitochondrial dysfunction.

METHODS: We analyzed levels of soluble HTT and HTT aggregates, as well as important fission and fusion proteins and mitochondrial respiratory chain activities, in quadriceps and heart of the R6/2 N-terminal fragment mouse model (12 weeks, 160±10 CAG repeats).

RESULTS: Soluble mutant HTT was present in both tissues with expression higher in cytoplasmic/mitochondrial than nuclear fractions. HTT aggregates were only detectable in R6/2 quadriceps, in association with increased levels of the pro-fission factor DRP1 and its phosphorylated active form, and decreased levels of the pro-fusion factor MFN2. In addition, respiratory chain complex activities were decreased. In heart that was without detectable HTT aggregates, we found no evidence for mitochondrial dysfunction.

CONCLUSION: Tissue specific factors may exist that protect the R6/2 heart from HTT aggregate formation and mitochondrial pathology.

**Keywords:** Huntingtin; mitochondria; fission and fusion; respiratory chain; skeletal muscle;

***Introduction***

Huntington's disease (HD) is a progressive movement disorder with dementia and behavioural abnormalities [1]. HD is caused by a CAG repeat expansion mutation in the huntingtin gene (*HTT*), encoding for the large huntingtin protein (HTT). Striatal and extra-striatal, e.g. cortical, degeneration constitutes the neuropathological signature of HD. However, HTT is ubiquitously expressed and there is also evidence indicating that mutant HTT causes a peripheral phenotype, for instance in skeletal muscle [2, 3].

The physiological function of wild-type HTT remains incompletely understood. HTT is predominantly found in the cytoplasm where it associates with the plasma membrane, mitochondria, lysosomes and the endoplasmatic reticulum [4-11]. Mutant HTT is predominantly localized in the cytoplasm but similar to wild-type HTT co-localizes also with the nucleus, endoplasmic reticulum, endosomes, Golgi-apparatus and mitochondria [12-15]. The mutation is thought to confer both a loss of physiological functions and a toxic gain of function, which is linked to the observation that mutant HTT species can form aggregates that may interfere with cellular functions [16].

In tissues of HD models, including skeletal muscle and in cells from HD patients, mitochondrial dysfunction involving disturbed calcium homoeostasis, enhanced reactive oxygen species (ROS) production and reduced biogenesis has repeatedly been reported [17]. HTT was shown to associate with DRP1 on the outer mitochondrial membrane increasing its enzymatic activity leading to increased mitochondrial fragmentation [18-21]. In addition, mutant HTT may associate with TIM23 influencing the effectiveness of mitochondrial import, which is important for the mitochondrial unfolded protein response ($UPR^{mt}$) [14]. Further to the direct influence of HTT on mitochondrial function, naturally occurring variability in genes relevant for fission and fusion significantly influenced motor age-at-onset independent of

the CAG repeat expansion [22]. These findings indicate that mutant HTT influences mitochondrial biology. No single role of HTT in mitochondrial function has emerged; however, several lines of evidence in different model systems and human material point towards a role in fission and fusion regulation [18-21, 23, 24], a key element in mitochondrial quality control. In support of this notion, reducing DRP1 activity in HD models improved the HD phenotype suggesting mitochondrial quality control pathways may be treatment targets for HD disease modification [20].

In the present study we investigated the relationship between the expression of full-length mutant HTT, the occurrence of HTT aggregates and mitochondrial biology in skeletal muscle and heart from the R6/2 fragment mouse model of HD. In contrast to brain, skeletal muscle is easy to access, including in humans. If a relationship existed between mutant HTT species and a biological phenotype in skeletal muscle, e.g. mitochondrial dysfunction, valuable insight into HD disease mechanisms could be gained with the potential to serve as peripheral biomarker. We hypothesised that 1) mutant HTT is expressed in skeletal muscle and heart; and 2) given the extant findings of increased mitochondrial fragmentation in HD models, and of mitochondrial abnormalities in skeletal muscle, that skeletal muscle and heart would show evidence of a shift of the fission and fusion balance towards mitochondrial fission, given that the N-terminal fragment model is a particularly aggressive model of HD.

***Materials and Methods***

*Animals*

R6/2 transgenic mice (B6CBATg(HDexon1)62Gpb/1J) and their corresponding wild-type B6CBAF1/J were purchased from Jackson Laboratory. The R6/2 fragment model contains exon 1 with expanded CAG repeats of the human *HTT* gene [25]. For genotyping and for determination of the CAG repeat length (160 ± 10) DNA was extracted from tail biopsies [26]. Mice at 12 weeks were sacrificed by cervical dislocation, quadriceps and heart were dissected and immediately snap-frozen in liquid nitrogen and stored at -80°C. For immunohistochemistry tissues were snap-frozen in liquid nitrogen-cooled 2-methylbutane and stored at -80°C. For electron microscopy 12 weeks-old mice were perfused with 4% paraformaldehyde and tissues were immediately fixed in 2.5% glutaraldehyde. All work was performed according to local regulations and EU Directive 2010/63/EU.

Animal care was in accordance with the United States Public Health Service Policy on Humane Care and Use of Laboratory Animals, and procedures were approved by the Institutional Animal and Use Committee of Psychogenics, Inc. (PHS OLAW animal welfare assurance number A4471-01), an AAALAC International accredited institution (Unit #001213) [27].

*Antibodies*

For western blotting the following antibodies were used: anti-DRP1 (dynamin-1-like protein, BD 611112) 1:1000 and anti-OPA1 (optic atrophy protein 1, BD 612606) 1:1000 from BD Biosciences. Anti-MFN1 (anti-mitofusin1, ab126575) 1:500, anti-MFN2 (mitofusin-2, ab50838) 1:1000; anti-NDUFA9 (NADH dehydrogenase [ubiquinone] 1 alpha subcomplex subunit 9, ab14713) 1:3000; anti-SDHA (succinate dehydrogenase [ubiquinone] flavoprotein

subunit, ab14715) 1:10000; anti-UQCRC2 (cytochrome b-$c_1$ complex subunit 2, ab14745) 1:6000; anti-MTCO1 (cytochrome c oxidase subunit 1, ab14705) 1:6000; anti-ATP5A (ab14748) 1:6000 and anti-citrate synthase (ab129095) 1:1000 from Abcam. For detection of the phosphorylation state anti-Phospho-DRP1 (Ser616) (3455, Cell Signaling) 1:1000 was used. For analysis of HTT aggregates the S829 (1:3000) antibody, kindly provided by Gillian Bates (UCL, UK), was used. As secondary antibodies goat anti-mouse IgG (H+L)-HRP (1:3000, 1706516, Bio-Rad), goat anti-rabbit IgG (H+L)-HRP (1:10000, 111-035-003, Jackson ImmunoResearch) or rabbit anti-goat IgG (H+L)-HRP (1:10000, R21459, Life Technologies) were used.

For immunohistochemistry the S829 antibody (1:400 in PBS, 5% horse serum, 0.05% Tween) and as secondary antibody donkey anti-sheep IgG (H+L) Alexa fluor 488 (1:400 in PBS, A11015, Thermo Fisher) were used.

*Total protein extraction, gel electrophoresis and western blot*

These methods were performed as described previously [28]. Tissues were lysed using a tissue lyser (Qiagen) in homogenization buffer (320 mM sucrose, 1 mM $K^+$ EDTA, 10 mM Tris/HCl, pH 7.4, 1 µg/ml pepstatin, 1 µg/ml leupeptin and 1 mM PMSF) followed by repeated centrifugation at 600×g at 4°C. The supernatant was used for protein analysis. For western blot analysis protein samples were denatured in NuPAGE LDL sample buffer (NP0008, Thermo Fisher) and analyzed on 9% Bis-Tris gels in MOPS buffer (50 mM MOPS, 50 mM Tris base, 0.2% SDS (w/v), 0.1 mM EDTA, pH 7.3) followed by western blotting on PVDF membranes in transfer buffer (25 mM bicine, 25 mM Bis-Tris, 1 mM EDTA, 20% methanol (v/v), pH 7.2). Analyses of HTT aggregates were performed on 6% Bis-Tris gels. Assembly of oxidative phosphorylation complexes was analyzed using blue native gel electrophoresis with 4%-16% gradient gels as described previously [29]. Protein extractions for analysis of

the phosphorylation state were performed in RIPA buffer (10 mM Tris base, 0.1% SDS (w/v), 1% Triton X-100 (v/v), 1% Na-deoxycholate (w/v), 5 mM EDTA, pH 7.4) containing phosphatase inhibitors (PhosSTOP, 04906837001, Sigma-Aldrich). For visualizing the total protein amount the membrane was incubated with Pierce Reversible Protein Stain Kit for PVDF membranes (Pierce, Rockford, USA) or Ponceau solution (2% Ponceau S (w/v), 3% trichloroacetic acid (w/v)) for nitrocellulose membranes (Bio-Rad). Data analysis was performed by densitometric quantification using the ImageQuant TL software (GE Healthcare). Protein levels were determined relative to total protein amount.

*Erenna Singulex SMC immunoassay for mutant HTT detection*

The MW1 antibody was developed by Dr. Paul Patterson [30]. 2B7 antibody generation and characterization were as previously described [31]. The 2B7 antibody was conjugated to magnetic particles (MPs), to a final concentration of 25 µg/mg of MPs, and the MW1 antibody was labeled to a final concentration of 1 µg/µl, using the Erenna capture and detection reagent labeling kits from Merck-Millipore, following the manufacturer's instructions. Conjugated/labeled antibodies were diluted in Assay Buffer (02-0474-00, Merck-Millipore) to 1:1200 and 1:4000, respectively, prior to performing the assay.

The immunoassay was largely performed as previously described [32]. In brief, mouse tissue samples were pre-diluted in artificial CSF (aCSF) with 1% Tween-20 (v/v) and complete protease inhibitor (11 697 498 001, Roche) to a concentration of 10 µg/ml of total protein. Pre-diluted tissue samples and 2B7 antibody coupled to MPs were added to assay buffer containing 6% BSA (w/v), 0.8% Triton X-100 (v/v), 750 mM NaCl and complete protease inhibitor in a 96-conical assay plate (P-96-450V-C, Axygen). The plate was sealed and incubated on a shaker at room temperature for 1 h. Samples were washed on a magnetic rack, using a HydroFlex Microplate 8 Channel Washer (Tecan), in 1x Erenna Wash Buffer (02-

0111-03, Merck-Millipore). Afterwards MPs were incubated with MW1 detection antibody for 1 h at room temperature. Samples were again washed in 1x Erenna Wash Buffer on a magnetic rack in a HydroFlex washer. The antibody-antigen complex was transferred to a new 96-conical assay plate to eliminate nonspecific binding events to the plastic. After buffer aspiration the Elution Buffer B (02-0297-00, Merck-Millipore) was added to the plate for 5 min of incubation while shaking. The eluted detection antibody was transferred to a Nunc 384-well analysis plate (264573, Sigma-Aldrich) and neutralized with Buffer D (02-0368-00, Merck-Millipore). The analysis plate was spun down to eliminate foaming and bubble formation, sealed, and subsequently analyzed with the Erenna Immunoassay System (Merck-Millipore).

*Subcellular fractionation*

For the Singulex assay tissues were lysed as described previously [33] but with buffer conditions suitable for the assay. All steps were performed on ice and at 4°C. 50 mg of tissue was minced using sharp scissors, suspended in 300 µl of STM buffer (250 mM sucrose, 50 mM Tris-HCl pH 7.4, 5 mM $MgCl_2$, 1 µg/ml pepstatin, 1 µg/ml leupeptin and 1 mM PMSF) and homogenized for 1 min at 1000 rpm using a Potter S homogenizer (Sartorius B. Braun). The homogenate was decanted into a 1.5-ml tube, remaining tissue fragments were re-suspended in 300 µl of STM buffer and homogenization was repeated. The homogenates were combined, incubated for 30 min on ice and vortexed for 15 sec. After taking 40 µl of the total lysate (TL) for analysis the homogenate was centrifuged for 15 min at 800×g. The pellet was the nuclear fraction and the supernatant the cytoplasmic/mitochondrial fraction. The pellet was washed in 300-500 µl of STM buffer, vortexed for 15 sec and centrifuged for 15 min at 500×g. The washing step was repeated and the pellet finally re-suspended in 200-500 µl of NET buffer (20 mM Hepes pH 7.9, 1.5 mM $MgCl_2$, 0.5 M NaCl, 0.2 mM EDTA, 1%

Triton X-100 (v/v), 1 µg/ml pepstatin, 1 µg/ml leupeptin and 1 mM PMSF). The nuclear fraction was lysed by sonification, centrifuged at 9,000×g for 30 min and the resultant supernatant was the final nuclear fraction (NF). The cytoplasmic/mitochondrial fraction was centrifuged at 800×g for 10 min to remove cell debris and the supernatant was the final cytoplasmic/mitochondrial fraction (CM). For subcellular fractionation into cytoplasmic and mitochondrial fractions, the cytoplasmic/mitochondrial fraction was further purified as described [33].

*Electron microscopy*

Two ultra-thin sections from different areas were used for electron microscopy. For quadriceps tissue the sections were prepared in longitudinal orientation to the fiber. Images of ultra-thin sections per sample were taken with a Jeol 1400 Transmission Electron Microscope (JEOL GmBH). For quantification five images per sample at ×12,000 magnification were used. Images were exported to a tablet-PC (iPad2, Apple) and the mitochondrial area and number were evaluated using the Glow Draw application (The Othernet, LLC © Daniel Cota), followed by quantification using ImageJ software (ImageJ 1.46r, Wayne Rasband, National Institutes of Health, USA). The median of individual results from each of the five images was calculated for the mitochondrial area and number [34]. Data acquisition and all analyses were done blinded to the genotype.

*Immunohistochemistry*

Quadriceps sections were cut in transverse orientation to the fiber direction at 10 µm. Sections were fixed for 10 min in acetone, washed with PBS followed by drying for 1 h at room temperature. The following procedures were performed in a humidified chamber: sections were blocked in blocking solution (5% goat serum (v/v) in PBS) for 45 min followed by incubation overnight at 4°C with the primary antibody. Sections were washed with PBS-T

(0.05% Tween (v/v) in PBS) and incubated with the secondary antibody for 1 h in the dark at room temperature. Sections were embedded in Citifluor AF1 (R1320, Agar Scientific) containing DAPI (5 µg/ml, DAPI dilactate, D3571, Life Technologies).

*mRNA isolation and quantitative real-time PCR*

mRNA was isolated with the RNeasyPlus Mini Kit (74134, Qiagen) and 2 µg of RNA was reverse-transcribed into cDNA with the iScript cDNA synthesis kit (Bio-Rad). Quantitative real-time PCR (qPCR) was performed using SYBR® green supermix with the CFX384 Touch Real-Time PCR Detection Systems (Bio-Rad) as previously described [28, 34]. Primer sequences are listed in supplementary tables S3. For gene expression analysis in muscle samples *Poldip3* (polymerase (DNA-directed), delta interacting protein 3) and *Metap1* (methionylaminopeptidase 1) were used as reference genes (R6/2 muscle: mean CV 0.17 and mean M Value 0.49), and *Sdha* (Succinate dehydrogenase [ubiquinone] flavoprotein subunit) and *Metap1* for heart samples (mean CV 0.16 and mean M Value 0.46). The reference genes were selected according to Hellemans and colleagues [35] with homogenous stable cDNA level mean CV < 0.25 and mean M value < 0.5. Data were analyzed with the Bio-Rad CFX manager software (Bio-Rad).

*Mitochondrial DNA copy number*

The DNA was isolated with Puregene Core Kit A (Qiagen) as instructed by the manufacturer. The mitochondrial DNA (mtDNA) copy number was determined with quantitative real-time PCR with the CFX384 Touch Real-Time PCR Detection Systems (Bio-Rad) as previously described [28]. For detection of the mtDNA the D-loop region was used. As reference *B2M* (beta-2-microglobulin) encoded on the nuclear DNA was used [36-38]. Primer sequences are listed in supplementary table S4.

*Enzyme activity assays*

Tissue lysates were prepared as described previously [28]. Briefly, extractions were performed in homogenization buffer (320 mM sucrose, 1 mM $K^+$ EDTA, 10 mM Tris/HCl, pH 7.4, 1 µg/ml pepstatin, 1 µg/ml leupeptin and 1 mM PMSF) using a tissue lyser (Qiagen) at 4°C. After centrifugation (600×g, 10 min at 4°C) the supernatant was used. Measurements of the activity of the respiratory chain enzyme complexes and of citrate synthase were performed as described previously [28, 39-42].

*ATP assay*

The amount of ATP was determined by using the ATP assay kit from Abcam (ab83555, abcam) as instructed by the manufacturer. The amount of ATP was calculated with the help of an ATP standard curve.

*Statistical analysis*

All data were evaluated blinded to the samples' genotype. Statistical analysis was performed using GraphPad Prism (version 5.00 for Windows, GraphPad Software, San Diego California USA). Data were examined for normal distribution using the Kolmogorov-Smirnov test. Parametric analysis of two groups was done with an unpaired *t*-test or with a Welch's unequal variances *t*-test. For non-parametric analysis of two groups the Mann-Whitney test was used. For analysis of three or more groups one-way ANOVA was performed.

***Results***

*Soluble mutant HTT is present in heart and quadriceps, while aggregates are only detectable in quadriceps*

We first examined whether soluble mutant HTT was expressed. Using the antibody combination 2B7/MW1 with the Singulex assay [31, 32, 43] there was clear evidence of soluble mutant HTT expression in total lysates of R6/2 transgenic (tg) quadriceps (Fig. 1A), and R6/2 heart muscle (Fig. 1D). We then investigated the distribution of total soluble mutant HTT in different cellular compartments. To this end we analyzed an enriched nuclear (NF) and cytoplasmic/mitochondrial fraction (CM) from quadriceps of R6/2 tg mice (Fig. 1B), and R6/2 tg heart (Fig. 1E). The cytoplasmic/mitochondrial fractions contained no detectable histone H3, a nuclear protein. The nuclear fractions were clearly enriched and contained no detectable GAPDH, a cytosolic protein, while some mitochondrial content remained since NDUFA9, a mitochondrial protein, was detectable at low levels. In R6/2 tg quadriceps (Fig. 1C) the cytoplasmic/mitochondrial fraction clearly contained more soluble mutant HTT than the nuclear fraction (R6/2 $P < 0.0001$). In R6/2 tg heart mutant HTT was only in the cytoplasmic/mitochondrial fraction detectable with western blot using the 1C2 antibody that binds to polyQ repeats [25, 44] (Fig. 1F).

The formation of HTT aggregates is a hallmark event in the pathogenesis of HD. We next examined whether HTT aggregates were detectable in quadriceps and heart muscle of R6/2 tg mice. To this end we used two different methods, immunohistochemistry and western blot. We used the S829 antibody, which was raised against the N-terminal exon 1 HTT protein and was shown to detect aggregates in R6/2 tg mice [45, 46]. In quadriceps of R6/2 tg mice aggregates were detectable on western blot (Fig. 2A) and also by confocal microscopy on tissue sections (Fig. 2B, G, Fig. S2). We then investigated the fractions

enriched for nuclear or cytoplasmic/mitochondrial content. This revealed that aggregates were present in quadriceps of R6/2 tg mice with levels much higher in the nuclear fraction than in the cytoplasmic/mitochondrial fraction (Fig. 2C). 3D analysis of a section using confocal microscopy with z-stacking also demonstrated aggregates predominantly near the nucleus but very often aggregates appeared in close vicinity to nuclei rather than within them (Fig. 2G).

In heart of R6/2 tg mice (Fig. 2D, E, Fig. S2), HTT aggregates were not evident using western blot or confocal microscopy. Furthermore aggregates were not detectable in the enriched nuclear or the cytoplasmic/mitochondrial fractions in heart of R6/2 tg mice (Fig. 2F).

*Fission and fusion protein imbalance is only observed in quadriceps of R6/2 tg mice*

Mitochondria form a dynamic network that undergoes fission and fusion to remain functional in the context of environmental and metabolic stress. Fission and fusion are mainly controlled by pro-fission and pro-fusion proteins. We investigated protein levels of the pro-fission dynamin-related protein (DRP1) and the pro-fusion proteins mitofusin 1 (MFN1), mitofusin 2 (MFN2) and optic atrophy 1 (OPA1) [47, 48] in quadriceps and heart of R6/2 mice. DRP1 protein levels were significantly increased in R6/2 tg quadriceps ($P < 0.01$; Fig. 3A, B), whereas MFN2 protein levels were decreased compared to wild-type (wt) mice ($P < 0.01$). OPA1 and MFN1 protein levels were similar in tg and wt mice. In contrast to quadriceps, in R6/2 heart fission and fusion protein levels were similar in tg and wt mice (Fig. 3C, D).

At the mRNA level, compared to wt, levels of *Dmn1l* and *Mfn1* were significantly increased in R6/2 tg quadriceps (*Dmn1l* $P < 0.01$; *Mfn1* $P < 0.01$), while *Opa1* mRNA level were decreased ($P < 0.0001$; Table 2). In R6/2 tg heart *Opa1* transcripts were decreased ($P < 0.05$). The poor

correlation of mRNA levels to protein levels can possibly be explained by post-transcriptional mechanisms involved in conversion of mRNA to protein, which are not well defined. In addition proteins may differ substantially in their *in vivo* half-life [49].

**Table 2.** Expression of mitochondrial pro-fission and pro-fusion genes

| **Relative mRNA level** | | ***Dmn1l*** | ***Opa1*** | ***Mfn1*** | ***Mfn2*** |
|---|---|---|---|---|---|
| **R6/2 quadriceps** | wt | 1.3 ± 0.07 | 1.4 ± 0.15 | 0.6 ± 0.07 | 0.7 ± 0.06 |
| **mean ± SEM** | tg | 1.7 ± 0.07 | 0.7 ± 0.05 | 1.0 ± 0.09 | 0.8 ± 0.08 |
| n ≥ 19 | *P* value | 0.0021[b] ** | <0.0001[a] *** | 0.0087[b] ** | 0.3432[a] ns |
| **R6/2 heart** | wt | 0.7 ± 0.09 | 0.9 ± 0.04 | 0.8 ± 0.05 | 0.8 ± 0.05 |
| **mean ± SEM** | tg | 0.7 ± 0.08 | 0.7 ± 0.07 | 1.0 ± 0.09 | 1.1 ± 0.13 |
| n ≥ 12 | *P* value | 0.4903[b] ns | 0.0138[b] * | 0.0541[a] ns | 0.0598[a] ns |

a) Welch's unequal variances *t*-test, b) Unpaired *t*-test

*Active phosphorylated DRP1 is increased only in quadriceps of R6/2 tg mice*

Absolute DRP1 protein levels do not necessarily reflect its enzymatic activity. The activity of DRP1 is regulated by a variety of post-translational modifications, including phosphorylation, *S*-nitrosylation, SUMO (small ubiquitin-like modifier)ylation, ubiquitination, and O-GlcNAcylation, in response to diverse cellular stimuli [50, 51]. Phosphorylation at the amino acid residue Ser616 (position in human DRP1) leads to DRP1 activation and mitochondrial fragmentation [52, 53]. Once activated, DRP1 is recruited from the cytosol to mitochondria to induce mitochondrial fragmentation [51, 54, 55]. We next examined the amount of active DRP1 by using an antibody, which detects active phosphorylated DRP1 (p-DRP1). To confirm the specificity of the antibody we first treated HEK293 cells with the protonophor CCCP (carbonyl cyanide *m*-chlorophenyl hydrazone) to induce fission [56]. We detected an

increase of p-DRP1, whereas absolute DRP1 level remained similar (Fig. S1), indicating that an increase in p-DRP1 signal reflects the increase of DRP1 enzymatic activity induced by CCCP.

In lysates of R6/2 tg quadriceps we observed increased p-DRP1 levels ($P < 0.01$) and an increased p-DRP1/DRP1 ratio compared to wt mice ($P < 0.05$) indicating that active DRP1 levels were elevated (Fig. 4A, B). We then performed subcellular fractionations for evaluating the distribution of DRP1 between the cytosolic and the mitochondrial compartment. DRP1 levels were higher in the quadriceps mitochondrial fractions of tg R6/2 mice (69 ± 7%) than those of wt (31 ± 10%; Fig. 4C, D). In heart of R6/2 tg mice levels of p-DRP1 were non-significantly lower ($P = 0.07$) in whole tissue lysates compared with wt; however, the p-DRP1/DRP1 ratio was similar in tg and wt hearts (Fig. 4E, F). In the mitochondrial fraction amounts of DRP1 were low with 8% in wt and 5% in tg hearts (Fig. 4G, H). In summary, higher levels of active DRP1 than in controls were only evident in tg quadriceps of R6/2 mice. In R6/2 heart tissue, the active DRP1/total DRP1 ratio was similar to controls.

*Mitochondrial mass*

Changes in the balance of mitochondrial pro-fission (p-DRP1/total DRP1) and pro-fusion factors (MFN1, MFN2, OPA1) can lead to abnormal mitochondrial network shape. We used electron microscopy to examine ultra-structural mitochondrial morphology and to analyze the size and number of mitochondria. We did not observe differences in cristae morphology in tg quadriceps or heart compared to wt (Fig. 5A, D). After quantification, we observed a non-significant increase in the amount of mitochondria in tg quadriceps of R6/2 mice ($P =$

0.07), whereas the size was similar to wt tissue (Fig. 5A-C). Mitochondrial size and number in R6/2 heart tg mice (Fig. 5D-F) were similar to controls (Fig. 5J-L).

In order to assess mitochondrial mass we analyzed citrate synthase activity, mitochondrial (mt) DNA copy number and *Tfam* (mitochondrial transcription factor A) mRNA expression or protein level. TFAM is an important regulator for mtDNA transcription and mtDNA copy number [57, 58]. Compared to wt tissue, citrate synthase activity, mtDNA copy number or *Tfam* mRNA levels were similar in R6/2 tg quadriceps and heart.

**Table 3.** Analysis of mitochondrial mass

| **Mitochondrial mass** | | **Citrate synthase activity/ total protein [µmol/min/mg]** | **Relative mtDNA copy number** | **Relative *Tfam* mRNA level** | **Relative TFAM protein level** |
|---|---|---|---|---|---|
| **R6/2 quadriceps** **mean ± SEM** n ≥ 6 | wt | 0.06 ± 0.01 | 0.7 ± 0.04[c] | 0.8 ± 0.14 | 1.1 ± 0.43 |
| | tg | 0.09 ± 0.02 | 0.8 ± 0.05[c] | 1.1 ± 0.20 | 0.87 ± 0.16 |
| | *P* value | 0.1496[b] ns | 0.4747[b] ns | 0.2741[a] ns | 0.57921[b] ns |
| **R6/2 heart** **mean ± SEM** n ≥ 6 | wt | 0.4 ± 0.05 | 0.7 ± 0.15 | 1.2 ± 0.17 | 0.8 ± 0.2 |
| | tg | 0.4 ± 0.02 | 0.9 ± 0.15 | 1.3 ± 0.11 | 1.2 ± 0.23 |
| | *P* value | 0.501[a] ns | 0.4283[b] ns | 0.655[b] ns | 0.1574[b] ns |

a) Welch's unequal variances *t*-test, b) Unpaired *t*-test, c) data were log-transformed

*The activity of complex I and complex IV is decreased in quadriceps of R6/2 tg mice*

An imbalance in mitochondrial fission and fusion can affect oxidative phosphorylation capacity and reduce ATP levels [59]. Therefore we next examined the activity of the respiratory chain complexes I, II/III and IV with spectrophotometry. To control for variations of mitochondrial mass we normalized our data to citrate synthase activity. In addition, we

examined ATP levels in all tissues. In R6/2 tg quadriceps we observed decreased complex I and complex IV activities ($P < 0.05$), whereas the activity of complex II/III was similar to wt (Fig. 6A). However, ATP levels were similar in tg and wt quadriceps (Fig. 6B). In tg heart tissue the respiratory chain activity and ATP levels were similar to wt (Fig. 6C, D).

In addition to the analysis of respiratory chain complex activities we assessed the assembly of the complexes using blue native gel electrophoresis. While the levels of most respiratory chain enzyme complexes were unaffected in R6/2 tg, levels of complex III assembly were increased in R6/2 tg quadriceps compared to wt ($P < 0.05$) (Table S1, S2).

***Discussion***

In this study we examined the subcellular localization of mutant HTT, and mitochondrial dynamics and function in skeletal and heart muscle of late-stage R6/2 mice. Soluble mutant HTT was present in both muscle tissues with soluble mutant HTT expression higher in cytoplasmic/mitochondrial than nuclear fractions. However, HTT aggregates were only detectable in R6/2 quadriceps, in association with increased levels of the pro-fission factor DRP1 and its phosphorylated active form, and decreased levels of the pro-fusion factor MFN2. In addition, respiratory chain complex activities were decreased. In heart, despite similarly high, or even higher, levels of soluble mutant HTT, there were no detectable HTT aggregates and no evidence for mitochondrial dysfunction. This suggests that R6/2 heart is protected from HTT aggregate formation and mitochondrial pathology.

We first used the very sensitive Singulex assay, to assess whether tissues contained mutant HTT [31, 32, 43]. This is important because hypotheses of HD related downstream biological consequences are based on the assumption that mutant HTT is expressed in the analyzed tissues. We showed that soluble mutant HTT was indeed present in R6/2 heart and skeletal muscle samples. This is consistent with studies showing that soluble mutant HTT is

expressed in a variety of non-CNS tissue of R6/2 tg mice e.g. skeletal muscle, liver and spleen [43].

We next examined soluble mutant HTT subcellular expression. We detected soluble mutant HTT in cytoplasmic/mitochondrial and in nuclear fractions and consistent with data from brains of R6/2 and *Hdh*Q150 mice, levels of HTT were highest in cytoplasmic/mitochondrial fractions [60, 61]. This indicates that full-length HTT, or fragments following cytoplasmic processing or CAG-repeat length-dependent aberrant splicing of *HTT* exon 1, can shuttle between the cytoplasm and the nucleus [12, 62-66]. It is unknown whether HTT contains a nuclear localization signal. However, HTT contains multiple HEAT (huntingtin, elongation factor 3, the PR65/A subunit of protein phosphatase 2A and the lipid kinase Tor) repeat sequences [67]. Proteins harboring HEAT domains often mediate protein-protein interactions and intracellular transport, including nucleocytoplasmic shuttling [68]. HTT contains a nuclear export signal (NES) in the C-terminal region, which is strictly conserved among species [62]. In addition HTT has within the first N-terminal 17 amino acids a translocated promoter region that acts as nuclear export signal [64]. Increasing polyQ expansions reduce its nuclear export and cause nuclear accumulation and aggregation of HTT [64]. The formation of intra-nuclear HTT aggregates is a pathological hallmark in human HD brains [70]. Therefore, we next examined whether our peripheral tissues contained aggregates. Consistent with previous findings we detected aggregates in total lysate of R6/2 exon 1 fragment model skeletal muscle but not heart [45, 71-73]. Also in *Hdh*Q150 mice aggregates have been detected in a wide range of peripheral tissues at 22 months of age, such as skeletal muscle, liver and kidney [74], while similar to our findings in heart of *Hdh*Q150 mice aggregates could not be identified [74]. In vitro studies have shown that aggregation will not occur until the monomer concentration exceeds a certain critical

concentration [75]. The aggregation process of the exon 1-derived fragment occurs in a time, concentration and polyQ repeat length dependent manner [75]. It is possible that N-terminal mutant exon 1-derived protein concentrations do not exceed that critical concentration in heart muscle samples. In contrast to in vitro aggregation kinetics [75] high amounts of soluble mutant HTT in vivo do not always correlate with the presence of aggregates. In R6/2 tg testis high level of the soluble form have been detected but no aggregates were observed. In contrast, other tissues with similar expression levels of soluble mutant HTT, as for example liver, were characterized by aggregate formation [43]. This discrepancy suggests that many factors such as the ability of cells to divide, cell specific expression levels and subcellular distribution of mutant HTT may determine whether aggregation occurs [76]. Furthermore, age-dependent aggregate formation may differ between tissues. In R6/2 tg mice aggregates have been detected in e.g. striatum at 2 weeks of age, in cortex at 4 weeks and in in skeletal muscle at 8 weeks of age. [45]. This supports the notion that some tissues are more prone to aggregation than others.

We found highest aggregate levels in the nuclear fraction of R6/2 skeletal muscle. However, HTT aggregates were often localized adjacent to the nuclei rather than within them, and cytoplasmic aggregates were also clearly present, similar to findings in cortex of zQ175 mice [69] and striatum of R6/2 mice [78]. Nuclear and cytoplasmic HTT aggregates can interfere with nucleocytoplasmic protein and mRNA transport, which has been shown in striatum and cortex of both R6/2 tg mice and zQ175, in human HD post-mortem brain tissue and in cell models expressing mutant *HTT* exon 1 [61, 69, 79]. Aggregate-mediated disruption of nucleocytoplasmic transport may thus be a critical event leading to pathology by affecting a number of cellular processes. We therefore next asked whether the presence of aggregates was associated with a biological phenotype. We investigated mitochondrial fission and

fusion given the evidence indicating fission and fusion imbalance in animal models and in human post-mortem brain [18, 19, 21, 23, 24]. Similar to aggregate formation, abnormal fission and fusion was limited to R6/2 skeletal muscle in which levels of total and activated DRP1 were increased, concomitant with reduced MFN2 levels, and a respiratory chain enzyme complex I and IV deficiency. This is similar to what has been observed in HD lymphoblasts and Hdh(Q111) striatal cells [19] lending further support to the notion of a shift of the fission and fusion balance towards fission in HD. In contrast, in R6/2 tg heart, in which there was no detectable aggregate formation, there was no evidence of any mitochondrial phenotype.

In summary, abnormal mitochondrial fission and fusion and respiratory chain defects were only evident in R6/2 tg skeletal muscle that had HTT aggregates. Fission and fusion maintain mitochondrial homeostasis and are essential for mitochondrial quality control [80]. Mitochondrial quality control is tightly associated with mitochondrial protein homeostasis which is maintained by mtUPR, a signaling pathway linking mitochondria with the nucleus [81]. Inhibition of the nucleocytoplasmic transport by mutant HTT aggregates may lead to severe defects in mitochondrial quality control pathways and impact the ability to respond to stress. The striking differences in aggregate formation and mitochondrial function between skeletal muscle and heart in the R6/2 model indicate that differences in these tissues may have a substantial modifying effect on HD pathogenesis. The underlying mechanisms of disease modification may warrant further exploration.

***Acknowledgements***

We thank Nathalie Birth, Jaqueline Hallitsch, Thomas Lenk and Medea Müller for technical assistance, and Dr Andreas Neueder for helpful comments on the manuscript. Further we

thank the animal facility and the electron microscopy unit (head Prof. Walther) at Ulm University for their help.

***Conflict of Interest statement***

We have no conflicts of interest.

***Funding***

This work was supported by CHDI Foundation (A-7328) to M.O.

## *References*


1. Ross, C.A., et al., *Huntington disease: natural history, biomarkers and prospects for therapeutics.* Nat Rev Neurol, 2014. **10**(4): p. 204-16.
2. Zielonka, D., et al., *Skeletal muscle pathology in Huntington's disease.* Front Physiol, 2014. **5**: p. 380.
3. van der Burg, J.M., M. Bjorkqvist, and P. Brundin, *Beyond the brain: widespread pathology in Huntington's disease.* Lancet Neurol, 2009. **8**(8): p. 765-74.
4. Panov, A.V., et al., *Early mitochondrial calcium defects in Huntington's disease are a direct effect of polyglutamines.* Nat Neurosci, 2002. **5**(8): p. 731-6.
5. Orr, A.L., et al., *N-terminal mutant huntingtin associates with mitochondria and impairs mitochondrial trafficking.* J Neurosci, 2008. **28**(11): p. 2783-92.
6. Kegel, K.B., et al., *Huntingtin expression stimulates endosomal-lysosomal activity, endosome tubulation, and autophagy.* J Neurosci, 2000. **20**(19): p. 7268-78.
7. Kegel, K.B., et al., *Huntingtin is present in the nucleus, interacts with the transcriptional corepressor C-terminal binding protein, and represses transcription.* J Biol Chem, 2002. **277**(9): p. 7466-76.
8. Strehlow, A.N., J.Z. Li, and R.M. Myers, *Wild-type huntingtin participates in protein trafficking between the Golgi and the extracellular space.* Hum Mol Genet, 2007. **16**(4): p. 391-409.
9. Choo, Y.S., et al., *Mutant huntingtin directly increases susceptibility of mitochondria to the calcium-induced permeability transition and cytochrome c release.* Hum Mol Genet, 2004. **13**(14): p. 1407-20.
10. Atwal, R.S., et al., *Huntingtin has a membrane association signal that can modulate huntingtin aggregation, nuclear entry and toxicity.* Hum Mol Genet, 2007. **16**(21): p. 2600-15.
11. Saudou, F. and S. Humbert, *The Biology of Huntingtin.* Neuron, 2016. **89**(5): p. 910-26.
12. Hoogeveen, A.T., et al., *Characterization and localization of the Huntington disease gene product.* Hum Mol Genet, 1993. **2**(12): p. 2069-73.
13. Imarisio, S., et al., *Huntington's disease: from pathology and genetics to potential therapies.* Biochem J, 2008. **412**(2): p. 191-209.
14. Yano, H., et al., *Inhibition of mitochondrial protein import by mutant huntingtin.* Nat Neurosci, 2014. **17**(6): p. 822-31.
15. Guo, X., et al., *VCP recruitment to mitochondria causes mitophagy impairment and neurodegeneration in models of Huntington's disease.* Nat Commun, 2016. **7**: p. 12646.
16. Davies, S.W., et al., *Formation of neuronal intranuclear inclusions underlies the neurological dysfunction in mice transgenic for the HD mutation.* Cell, 1997. **90**(3): p. 537-48.
17. Costa, V. and L. Scorrano, *Shaping the role of mitochondria in the pathogenesis of Huntington's disease.* EMBO J, 2012. **31**(8): p. 1853-64.
18. Song, W., et al., *Mutant huntingtin binds the mitochondrial fission GTPase dynamin-related protein-1 and increases its enzymatic activity.* Nat Med, 2011. **17**(3): p. 377-82.
19. Costa, V., et al., *Mitochondrial fission and cristae disruption increase the response of cell models of Huntington's disease to apoptotic stimuli.* EMBO Mol Med, 2010. **2**(12): p. 490-503.
20. Guo, X., et al., *Inhibition of mitochondrial fragmentation diminishes Huntington's disease-associated neurodegeneration.* J Clin Invest, 2013. **123**(12): p. 5371-88.
21. Shirendeb, U.P., et al., *Mutant huntingtin's interaction with mitochondrial protein Drp1 impairs mitochondrial biogenesis and causes defective axonal transport and synaptic degeneration in Huntington's disease.* Hum Mol Genet, 2012. **21**(2): p. 406-20.
22. Genetic Modifiers of Huntington's Disease, C., *Identification of Genetic Factors that Modify Clinical Onset of Huntington's Disease.* Cell, 2015. **162**(3): p. 516-26.
23. Shirendeb, U., et al., *Abnormal mitochondrial dynamics, mitochondrial loss and mutant huntingtin oligomers in Huntington's disease: implications for selective neuronal damage.* Hum Mol Genet, 2011. **20**(7): p. 1438-55.

24. Kim, J., et al., *Mitochondrial loss, dysfunction and altered dynamics in Huntington's disease.* Hum Mol Genet, 2010. **19**(20): p. 3919-35.
25. Mangiarini, L., et al., *Exon 1 of the HD gene with an expanded CAG repeat is sufficient to cause a progressive neurological phenotype in transgenic mice.* Cell, 1996. **87**(3): p. 493-506.
26. Mangiarini, L., et al., *Exon 1 of the HD Gene with an Expanded CAG Repeat Is Sufficient to Cause a Progressive Neurological Phenotype in Transgenic Mice.* Cell, 1996. **87**: p. 493-506.
27. Menalled, L.B., et al., *Comprehensive behavioral and molecular characterization of a new knock-in mouse model of Huntington's disease: zQ175.* PLoS One, 2012. **7**(12): p. e49838.
28. Hering, T., et al., *Selective striatal mtDNA depletion in end-stage Huntington's disease R6/2 mice.* Exp Neurol, 2015. **266**: p. 22-9.
29. Schagger, H. and G. von Jagow, *Blue native electrophoresis for isolation of membrane protein complexes in enzymatically active form.* Anal Biochem, 1991. **199**(2): p. 223-31.
30. Ko, J., S. Ou, and P.H. Patterson, *New anti-huntingtin monoclonal antibodies: implications for huntingtin conformation and its binding proteins.* Brain Res Bull, 2001. **56**(3-4): p. 319-29.
31. Weiss, A., et al., *Single-step detection of mutant huntingtin in animal and human tissues: a bioassay for Huntington's disease.* Anal Biochem, 2009. **395**(1): p. 8-15.
32. Wild, E.J., et al., *Quantification of mutant huntingtin protein in cerebrospinal fluid from Huntington's disease patients.* J Clin Invest, 2015. **125**(5): p. 1979-86.
33. Dimauro, I., et al., *A simple protocol for the subcellular fractionation of skeletal muscle cells and tissue.* BMC Res Notes, 2012. **5**: p. 513.
34. Hering, T., et al., *Mitochondrial cristae remodelling is associated with disrupted OPA1 oligomerisation in the Huntington's disease R6/2 fragment model.* Exp Neurol, 2017. **288**: p. 167-175.
35. Hellemans, J., et al., *qBase relative quantification framework and software for management and automated analysis of real-time quantitative PCR data.* Genome Biol, 2007. **8**(2): p. R19.
36. Giorgetti, E., et al., *Rescue of Metabolic Alterations in AR113Q Skeletal Muscle by Peripheral Androgen Receptor Gene Silencing.* Cell Rep, 2016. **17**(1): p. 125-36.
37. Wai, T., et al., *The role of mitochondrial DNA copy number in mammalian fertility.* Biol Reprod, 2010. **83**(1): p. 52-62.
38. Bai, R.K. and L.J. Wong, *Simultaneous detection and quantification of mitochondrial DNA deletion(s), depletion, and over-replication in patients with mitochondrial disease.* J Mol Diagn, 2005. **7**(5): p. 613-22.
39. King, T.E., F.C. Yong, and S. Takemori, *Studies on cytochrome oxidase. 3. Ligand reactions and Schiff base formation of heme a.* J Biol Chem, 1967. **242**(5): p. 819-29.
40. Moreadith, R.W., et al., *Congenital deficiency of two polypeptide subunits of the iron-protein fragment of mitochondrial complex I.* The Journal of Clinical Investigation, 1987. **79**(2): p. 463-467.
41. Wharton, D.C. and A. Tzagoloff, *[45] Cytochrome oxidase from beef heart mitochondria.* Methods in Enzymology, 1967. **10**: p. 245-250.
42. Coore, H.G., et al., *Regulation of adipose tissue pyruvate dehydrogenase by insulin and other hormones.* Biochem J, 1971. **125**(1): p. 115-27.
43. Baldo, B., et al., *TR-FRET-based duplex immunoassay reveals an inverse correlation of soluble and aggregated mutant huntingtin in huntington's disease.* Chem Biol, 2012. **19**(2): p. 264-75.
44. Trottier, Y., et al., *Polyglutamine expansion as a pathological epitope in Huntington's disease and four dominant cerebellar ataxias.* Nature, 1995. **378**(6555): p. 403-6.
45. Sathasivam, K., et al., *Identical oligomeric and fibrillar structures captured from the brains of R6/2 and knock-in mouse models of Huntington's disease.* Hum Mol Genet, 2010. **19**(1): p. 65-78.
46. Sathasivam K, W.B., Mahal A, Bertaux F, Wanker EE, Shima DT, Bates GP., *Centrosome disorganization in fibroblast cultures derived from R6/2 Huntington's disease (HD) transgenic mice and HD patients.* Hum Mol Genet, 2001. **10**(21): p. 2425-35.

47. Westermann, B., *Mitochondrial fusion and fission in cell life and death.* Nat Rev Mol Cell Biol, 2010. **11**(12): p. 872-84.
48. Westermann, B., *Bioenergetic role of mitochondrial fusion and fission.* Biochim Biophys Acta, 2012. **1817**(10): p. 1833-8.
49. Greenbaum, D., et al., *Comparing protein abundance and mRNA expression levels on a genomic scale.* Genome Biol, 2003. **4**(9): p. 117.
50. Chang, C.R. and C. Blackstone, *Dynamic regulation of mitochondrial fission through modification of the dynamin-related protein Drp1.* Ann N Y Acad Sci, 2010. **1201**: p. 34-9.
51. Otera, H., N. Ishihara, and K. Mihara, *New insights into the function and regulation of mitochondrial fission.* Biochim Biophys Acta, 2013. **1833**(5): p. 1256-68.
52. Shahni, R., et al., *Signal transducer and activator of transcription 2 deficiency is a novel disorder of mitochondrial fission.* Brain, 2015. **138**(Pt 10): p. 2834-46.
53. Perdiz, D., et al., *Stress-induced hyperacetylation of microtubule enhances mitochondrial fission and modulates the phosphorylation of Drp1 at 616Ser.* Cell Signal, 2017. **39**: p. 32-43.
54. Palmer, C.S., et al., *MiD49 and MiD51, new components of the mitochondrial fission machinery.* EMBO Rep, 2011. **12**(6): p. 565-73.
55. Liu, R. and D.C. Chan, *The mitochondrial fission receptor Mff selectively recruits oligomerized Drp1.* Mol Biol Cell, 2015. **26**(24): p. 4466-77.
56. Head, B., et al., *Inducible proteolytic inactivation of OPA1 mediated by the OMA1 protease in mammalian cells.* J Cell Biol, 2009. **187**(7): p. 959-66.
57. Falkenberg, M., et al., *Mitochondrial transcription factors B1 and B2 activate transcription of human mtDNA.* Nat Genet, 2002. **31**(3): p. 289-94.
58. Falkenberg, M., N.G. Larsson, and C.M. Gustafsson, *DNA replication and transcription in mammalian mitochondria.* Annu Rev Biochem, 2007. **76**: p. 679-99.
59. Chen, H., et al., *Mitochondrial fusion is required for mtDNA stability in skeletal muscle and tolerance of mtDNA mutations.* Cell, 2010. **141**(2): p. 280-9.
60. Landles, C., et al., *Proteolysis of mutant huntingtin produces an exon 1 fragment that accumulates as an aggregated protein in neuronal nuclei in Huntington disease.* J Biol Chem, 2010. **285**(12): p. 8808-23.
61. Grima, J.C., et al., *Mutant Huntingtin Disrupts the Nuclear Pore Complex.* Neuron, 2017. **94**(1): p. 93-107 e6.
62. Xia, J., et al., *Huntingtin contains a highly conserved nuclear export signal.* Hum Mol Genet, 2003. **12**(12): p. 1393-403.
63. Benn, C.L., et al., *Contribution of nuclear and extranuclear polyQ to neurological phenotypes in mouse models of Huntington's disease.* Hum Mol Genet, 2005. **14**(20): p. 3065-78.
64. Cornett, J., et al., *Polyglutamine expansion of huntingtin impairs its nuclear export.* Nat Genet, 2005. **37**(2): p. 198-204.
65. Sathasivam K, N.A., Gipson TA, Landles C, Benjamin AC, Bondulich MK, Smith DL, Faull RL, Roos RA, Howland D, Detloff PJ, Housman DE, Bates GP, *Aberrant splicing of Htt generates the pathogenic exon 1 protein in HD.* Proc Natl Acad Sci U S A, 2013. **110**(6): p. 2366-70.
66. Neueder, A., et al., *The pathogenic exon 1 HTT protein is produced by incomplete splicing in Huntington's disease patients.* Sci Rep, 2017. **7**(1): p. 1307.
67. Li, W., et al., *Expression and characterization of full-length human huntingtin, an elongated HEAT repeat protein.* J Biol Chem, 2006. **281**(23): p. 15916-22.
68. Neuwald, A.F. and T. Hirano, *HEAT repeats associated with condensins, cohesins, and other complexes involved in chromosome-related functions.* Genome Res, 2000. **10**(10): p. 1445-52.
69. Gasset-Rosa, F., et al., *Polyglutamine-Expanded Huntingtin Exacerbates Age-Related Disruption of Nuclear Integrity and Nucleocytoplasmic Transport.* Neuron, 2017. **94**(1): p. 48-57 e4.
70. DiFiglia, M., et al., *Aggregation of huntingtin in neuronal intranuclear inclusions and dystrophic neurites in brain.* Science, 1997. **277**(5334): p. 1990-3.
71. Orth, M., et al., *Inclusion formation in Huntington's disease R6/2 mouse muscle cultures.* Journal of Neurochemistry, 2003. **87**(1): p. 1-6.

72. Sathasivam, K., et al., *Formation of polyglutamine inclusions in non-CNS tissue.* Hum Mol Genet, 1999. **8**(5): p. 813-22.
73. Mielcarek, M., et al., *Dysfunction of the CNS-heart axis in mouse models of Huntington's disease.* PLoS Genet, 2014. **10**(8): p. e1004550.
74. Moffitt, H., et al., *Formation of polyglutamine inclusions in a wide range of non-CNS tissues in the HdhQ150 knock-in mouse model of Huntington's disease.* PLoS One, 2009. **4**(11): p. e8025.
75. Scherzinger, E., et al., *Self-assembly of polyglutamine-containing huntingtin fragments into amyloid-like fibrils: implications for Huntington's disease pathology.* Proc Natl Acad Sci U S A, 1999. **96**(8): p. 4604-9.
76. Bates, G., *Huntingtin aggregation and toxicity in Huntington's disease.* Lancet, 2003. **361**(9369): p. 1642-4.
77. Weiss, A., et al., *Mutant huntingtin fragmentation in immune cells tracks Huntington's disease progression.* J Clin Invest, 2012. **122**(10): p. 3731-6.
78. Kurosawa, M., et al., *Depletion of p62 reduces nuclear inclusions and paradoxically ameliorates disease phenotypes in Huntington's model mice.* Hum Mol Genet, 2015. **24**(4): p. 1092-105.
79. Woerner, A.C., et al., *Cytoplasmic protein aggregates interfere with nucleocytoplasmic transport of protein and RNA.* Science, 2016. **351**(6269): p. 173-6.
80. Andreux, P.A., R.H. Houtkooper, and J. Auwerx, *Pharmacological approaches to restore mitochondrial function.* Nat Rev Drug Discov, 2013. **12**(6): p. 465-83.
81. Jovaisaite, V., L. Mouchiroud, and J. Auwerx, *The mitochondrial unfolded protein response, a conserved stress response pathway with implications in health and disease.* J Exp Biol, 2014. **217**(Pt 1): p. 137-43.
82. Ciammola, A., et al., *Increased apoptosis, Huntingtin inclusions and altered differentiation in muscle cell cultures from Huntington's disease subjects.* Cell Death Differ, 2006. **13**(12): p. 2068-78.
83. Saft, C., et al., *Mitochondrial impairment in patients and asymptomatic mutation carriers of Huntington's disease.* Mov Disord, 2005. **20**(6): p. 674-9.

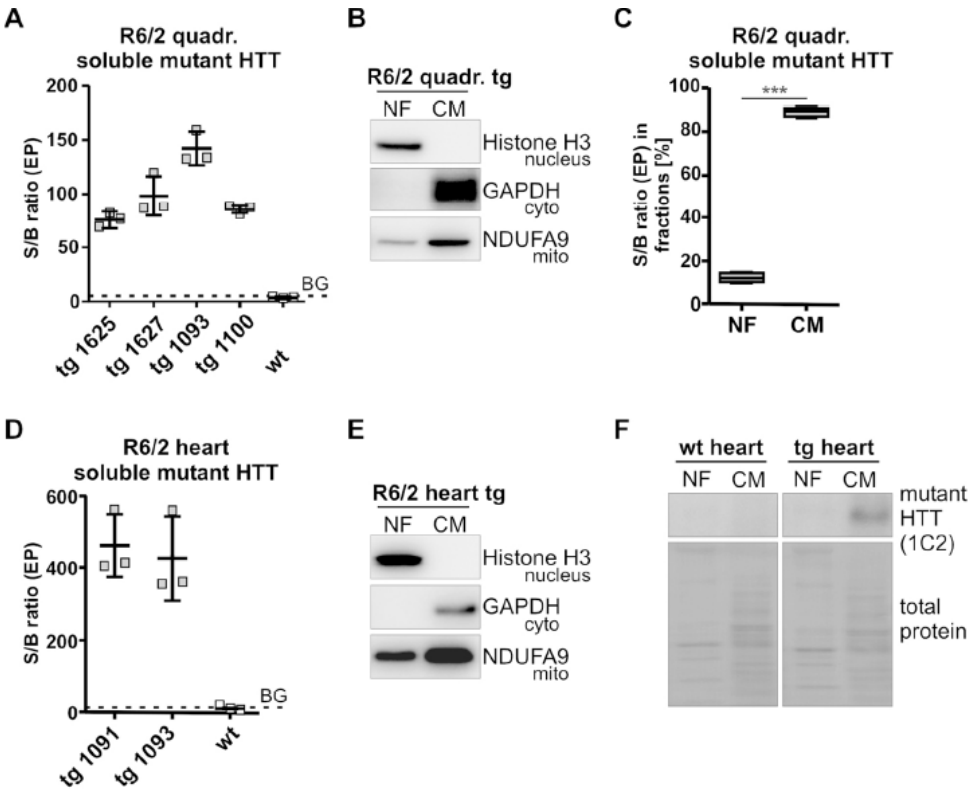


Figure 1. Soluble mutant HTT is detectable in quadriceps and heart of R6/2 mice.
A) Singulex assay for soluble mutant HTT analysis in quadriceps. Data are presented as scatter plot with means ± SD from N=3 technical replicates. Due to technical replicates data were evaluated without statistical analysis. B) Representative western blots of subcellular fractionations of quadriceps. Purity of the fractions was analyzed by histone H3 (nuclear protein), GAPDH (cytosolic protein) and NDUFA9 (mitochondrial protein). C) Singulex assay for soluble mutant HTT analysis of subcellular fractions. Data are presented as box plots with whiskers from minimum to maximum from n=4. Statistical test: t-test, ***P < 0.0001. D) Singulex assay for soluble mutant HTT analysis in heart. Data are presented as scatter plot with means ± SD from N=3 technical replicates. E) Representative western blots of subcellular fractionations of heart. Purity of the fractions was analyzed using the same antibodies as in B). F) Western blots of R6/2 heart of subcellular fractions using the 1C2 antibody detecting polyQ repeats. Antibody characterization and full-length blots are shown in figure S3.
Abbreviations: Quadr.: quadriceps, wt: wild-type mice, tg: transgenic mice, NF: nuclear fraction, CM: cytoplasmic/mitochondrial fraction, BG: background

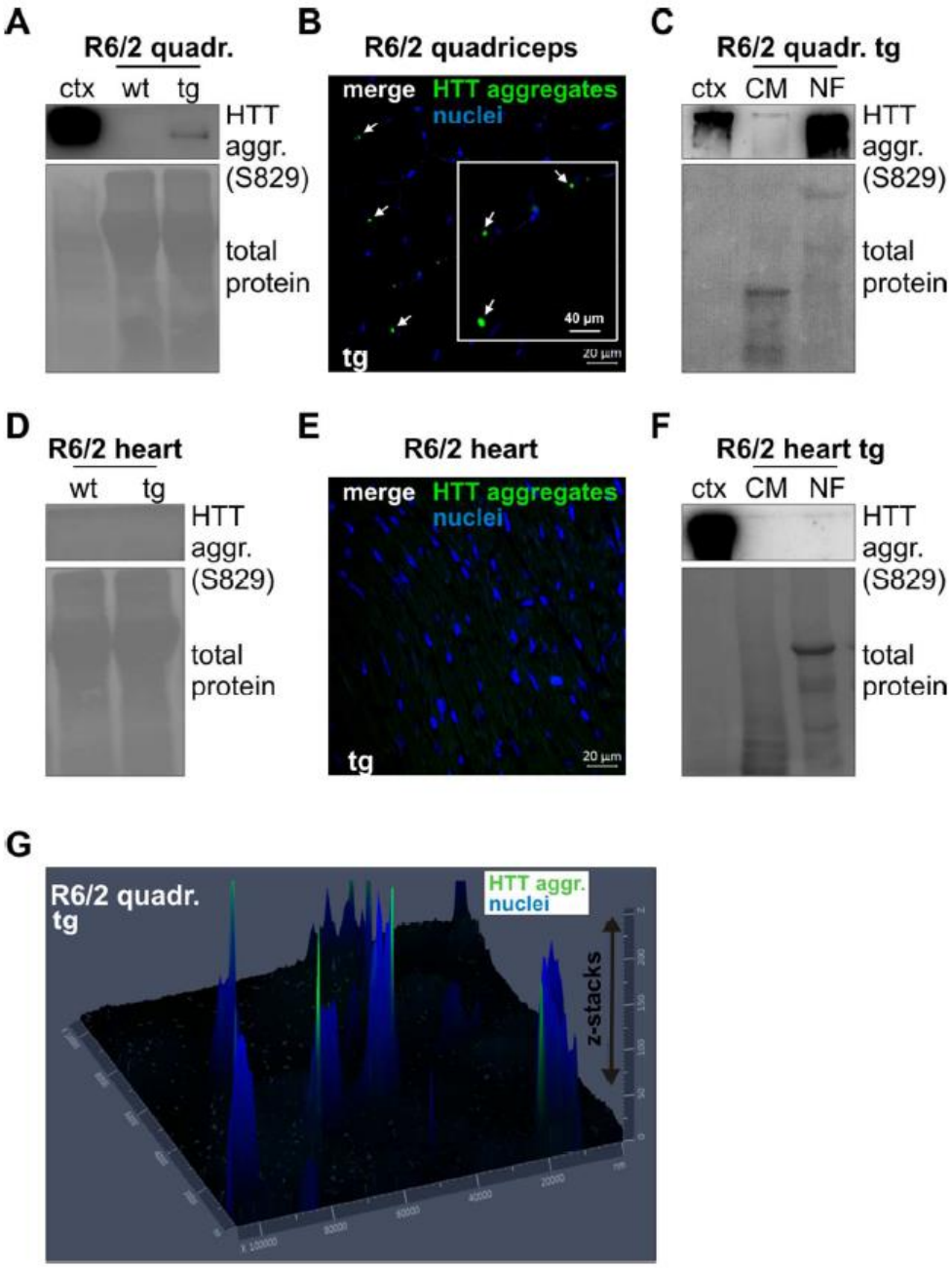


Figure 2. HTT aggregates are detectable only in quadriceps of R6/2 tg mice.
A) Western blots of quadriceps lysates analyzing HTT aggregates using the S829 antibody. HTT aggregates were detected in the stacking gel. Cortex lysates of R6/2 tg mice were used as antibody control. The total protein amount was detected with Ponceau S solution. B) Immunohistochemistry of quadriceps tissue sections. HTT aggregates were detected with the S829 antibody. Primary antibodies were detected with Alexa 488 nm conjugated secondary antibodies and nuclei were detected with DAPI. HTT aggregates are indicated by arrows. C) Western blots of subcellular fractionations analyzing HTT aggregates in quadriceps using the S829 antibody. The total protein was stained with Ponceau S solution. Cortex lysates of R6/2 tg mice were used as antibody control. D) Western blots of heart lysates analyzing HTT aggregates using the S829 antibody. The total protein was stainedwith Ponceau S solution. E) Immunohistochemistry of heart tissue sections done as in B). F) Western blots of subcellular fractionations analyzing HTT aggregates in heart using the S829 antibody. The total protein amount was detected with Ponceau S solution. Cortex lysates of R6/2 tg mice were used as antibody control. G) Immunohistochemistry of HTT aggregates in

quadriceps: 3D analysis of a section using confocal microscopy with z-stacking. Antibody characterization and full-length blots are shown in figure S3.
Abbreviations: Quadr.: quadriceps, wt: wild-type mice, tg: transgenic mice, aggr.: aggregates, ctx: cortex tissue lysates of R6/2 transgenic mice, NF: nuclear fraction, CM: cytoplasmic/mitochondrial fraction

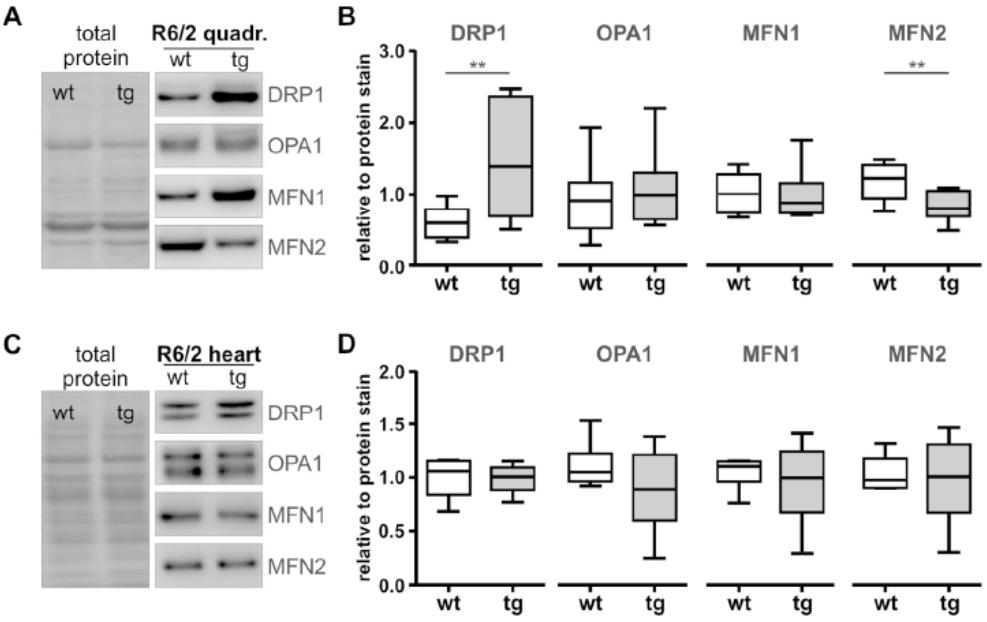


Figure 3. Fission and fusion protein levels are imbalanced only in quadriceps of R6/2 tg mice.
A-D) Representative western blots (A, C) and quantification (B, D) of fission (DRP1) and fusion (OPA1, MFN1, MFN2) proteins in quadriceps (A, B) or heart (C, D) of R6/2 mice. Protein levels were normalized to total protein stain. Data are presented as box plots with whiskers from minimum to maximum from n ≥ 9 (B) or n=6 (D). Statistical test: t-test or Welch's unequal variances t-test (for DRP1 quadriceps), **P < 0.001. Antibody characterization and full-length blots are shown in figure S4.
Abbreviations: Quadr.: quadriceps, wt: wild-type mice, tg: transgenic mice

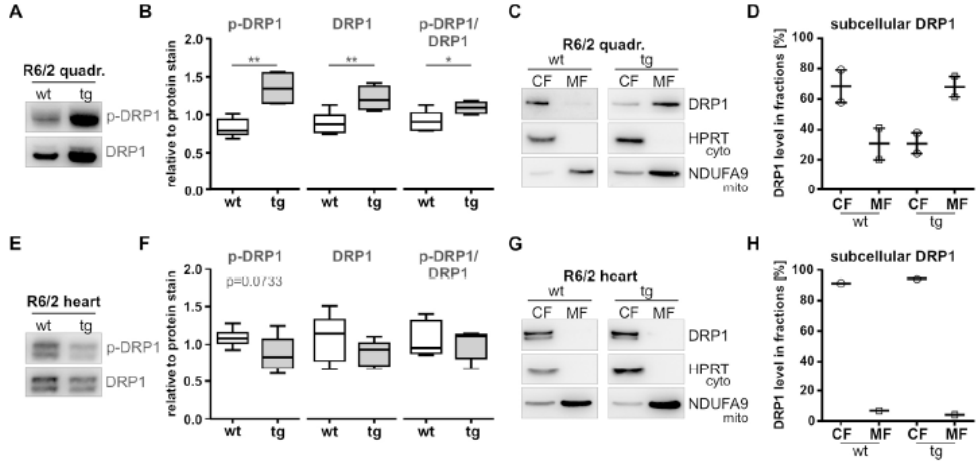


Figure 4. Active DRP1 levels are increased only in quadriceps of R6/2 tg mice.
A, B) Representative western blots (A) and quantification (B) of quadriceps using the p-DRP1 (DRP1-Ser616) and DRP1 antibody. Protein levels were normalized to total protein stain or a ratio of p-DRP1 to DRP1 was calculated. Data are presented as box plots with whiskers from minimum to maximum from n ≥ 4. Statistical test: t-test, *P < 0.05, **P < 0.001. C) Representative western blots of subcellular fractions of quadriceps using HPRT as cytosolic and NDUFA9 as mitochondrial marker. D) Quantification of DRP1 level in subcellular fractions of quadriceps. Data are presented as scatter plot with means ± SEM from n=2. Due to low sample number data were evaluated without statistical analysis. E, F) Representative western blots (E) and quantification (F) of heart using the p-DRP1 (DRP1-Ser616) and DRP1 antibody. Protein levels were normalized to total protein stain or a ratio of p-DRP1 to DRP1 was calculated. Data are presented as box plots with whiskers from minimum to maximum from n ≥ 5. Statistical test: t-test, P ≤ 0.1 is indicated by the corresponding P-value. G) Western blots of subcellular fractions of heart using same antibodies as in C). H) Quantification of DRP1 level in subcellular fractions of heart. Data are presented from n=1 and were evaluated without statistical analysis. Antibody characterization and full-length blots are shown in figure S4.
Abbreviations: Quadr.: quadriceps, wt: wild-type mice, tg: transgenic mice, CF: cytoplasmic fraction, MF: mitochondrial fraction

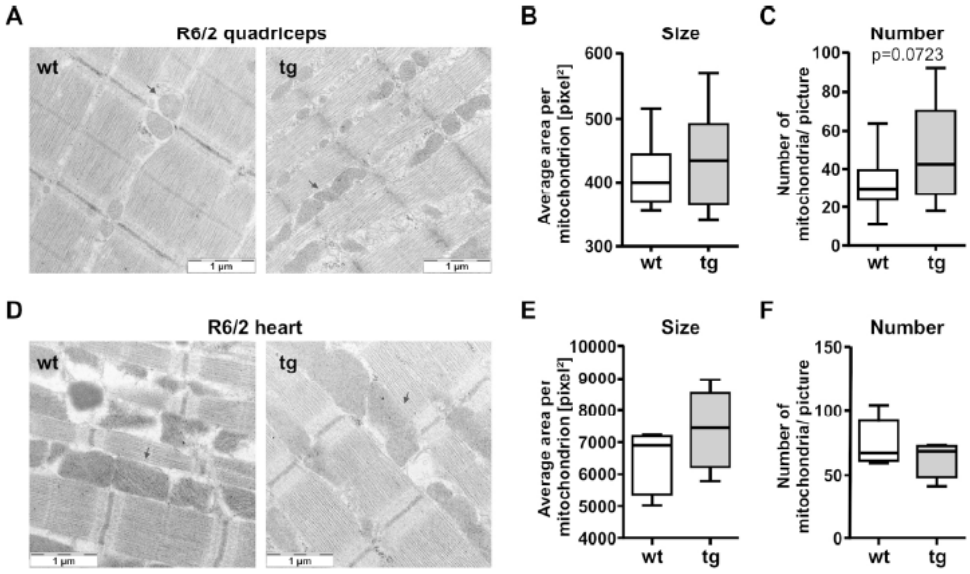


Figure 5. Electron microscopy of mitochondria.
A-C) Analysis of mitochondrial shape and number of quadriceps. Electron microscopic images of quadriceps with 40,000× magnification, mitochondria are indicated by arrows (A). The mitochondrial size is presented as average area per mitochondrion in pixel2 (B), the number of mitochondria is presented as mitochondria per picture (C). For quantitative analysis five images per sample at 12,000× magnification was used. For quadriceps tissue the sections for electron microscopy were prepared in longitudinal orientation to the fiber. D-F) Analysis of mitochondrial shape and number of heart. Electron microscopic images of quadriceps with 40,000× magnification, mitochondria are indicated by arrows (D). The mitochondrial size is presented as average area per mitochondrion in pixel2 (E), the number of mitochondria is presented as mitochondria per picture (F). Data are presented as box plots with whiskers from minimum to maximum from n = 10 (B and C) and n ≥ 5 (E and F). Statistical test: t-test, P ≤ 0.1 is indicated by the corresponding P-value.
Abbreviations: Quadr.: quadriceps, wt: wild-type mice, tg: transgenic mice

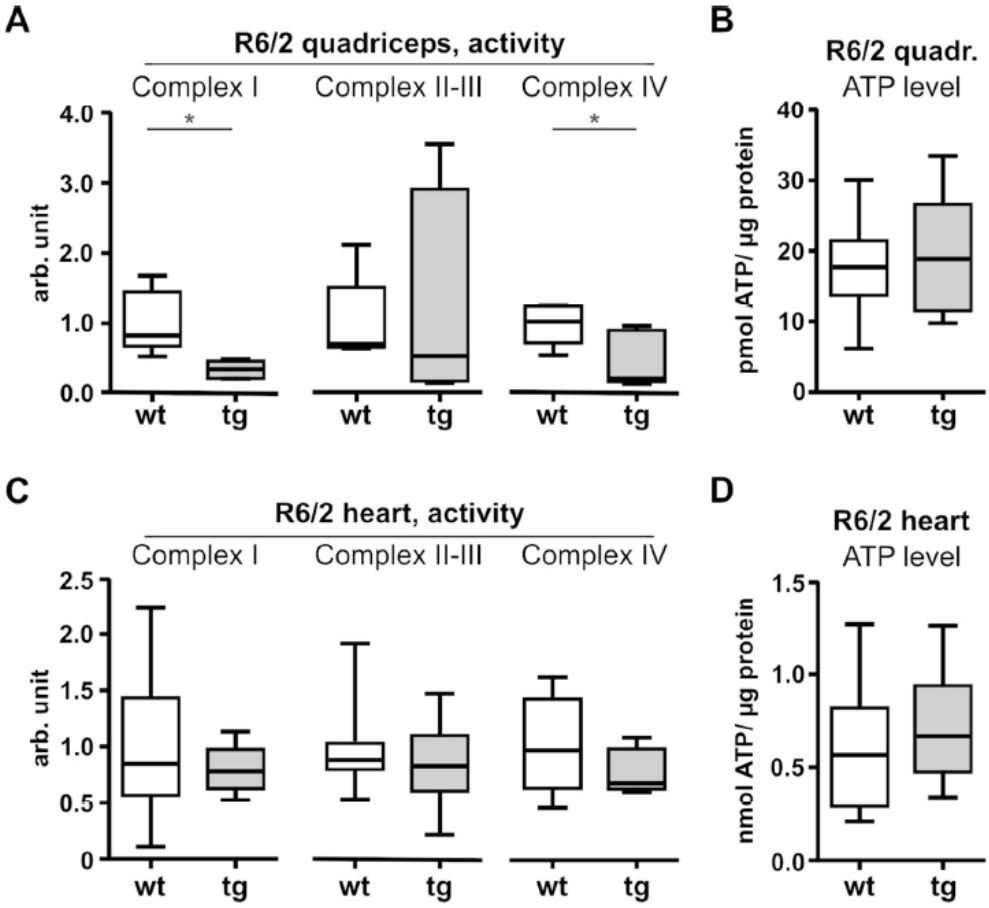


Figure 6. Activity of respiratory chain complex I and complex IV is decreased in quadriceps of R6/2 tg mice. A) Complex I, complex II-III and complex IV activities of quadriceps of R6/2 mice. Activities were normalized to citrate synthase activities and to each wt. B) ATP level in quadriceps of R6/2 mice. C) Complex I, complex II-III and complex IV activities of heart of R6/2 mice. Activities were normalized to citrate synthase activities and to each wt. D) ATP level in heart. Data are presented as box plots with whiskers from minimum to maximum from $n \geq 4$ (A and B) or $n \geq 7$ (C and D). Statistical test: t-test or Welch's unequal variances t-test (complex I and complex IV activity in heart), *$P < 0.05$.
Abbreviations: Quadr.: quadriceps, wt: wild-type mice, tg: transgenic mice